MITSUBISHI ELECTRIC RESEARCH LABORATORIES
https://www.merl.com

Automotive Radar Interference Mitigation with Fast-Time-Frequency Mode Retrieval

Jin, Sian; Pu, Wang; Boufounos, Petros T.; Orlik, Philip V.; Roy, Sumit

TR2022-029 April 05, 2022

Abstract

This paper considers mutual interference mitigation (MIM) for frequency modulated continuous wave (FMCW) automotive radar. Particularly, we exploit distinguished features of target and interference components in the fast-time-frequency (fTF) representation and, as opposed to existing fast-time MIM methods on nulling the interference component, propose to directly recover the underwhelmed target component via the fast-time-frequency mode retrieval (fTFMR). This is achieved by utilizing the Fourier synchrosqueezed transform (FSST) and introducing robust ridge detection that, in combination, guarantees that the recovered fast-time errors of the target signal are bounded at separable time intervals. Comprehensive performance comparison with a list of baseline methods shows that the proposed MIM method yields higher output signal-to- interference-noise ratios (SINRs) at both the range and velocity domains and reduces the false alarm.

IEEE Radar Conference (RadarCon) 2022

Mitsubishi Electric Research Laboratories, Inc.
201 Broadway, Cambridge, Massachusetts 02139

Automotive Radar Interference Mitigation with Fast-Time-Frequency Mode Retrieval

Sian Jin†*, Pu Wang†, Petros Boufounos†, Phil Orlik†, and Sumit Roy*
†Mitsubishi Electric Research Laboratories (MERL), Cambridge, MA, USA
*Department of Electrical & Computer Engineering, University of Washington, Seattle, WA, USA

***Abstract*—This paper considers mutual interference mitigation (MIM) for frequency modulated continuous wave (FMCW) automotive radar. Particularly, we exploit distinguished features of target and interference components in the fast-time-frequency (fTF) representation and, as opposed to existing fast-time MIM methods on nulling the interference component, propose to directly recover the underwhelmed target component via the fast-time-frequency mode retrieval (fTFMR). This is achieved by utilizing the Fourier synchrosqueezed transform (FSST) and introducing robust ridge detection that, in combination, guarantees that the recovered fast-time errors of the target signal are bounded at separable time intervals. Comprehensive performance comparison with a list of baseline methods shows that the proposed MIM method yields higher output signal-to-interference-noise ratios (SINRs) at both the range and velocity domains and reduces the false alarm.**

I. Introduction

Intelligent vehicles are equipped with more and more radar sensors for full-view, all-weather perception. New signaling schemes such as phase modulated continuous wave (PMCW) [1] and orthogonal frequency-division multiplexing (OFDM) [2] have shown better capabilities than the traditional frequency modulated continuous wave (FMCW) scheme, at a price of significantly higher sampling rates and increased requirements for transceiver hardware [3]–[6]. Nevertheless, the FMCW scheme remains the mainstream option to achieve full four-dimensional (range-velocity-azimuth-elevation) automotive radar with a sub-degree angular resolution at a mass production level.

For the FMCW-based automotive radar operating in the same regulated frequency bands (e.g., 77-81 GHz), radar interference needs to be addressed. Otherwise, it raises noise floor, jams receiver antennas, triggers false alarms, and causes missing detection [2]. Mutual interference mitigation (MIM) has received attention over past few years. Recent developments can be divided into several categories: 1) fast-time domain MIM [7]–[16] such as interference-zeroing [8], adaptive noise cancellers [9] and sparse sampling [10]; 2) slow-time domain MIM such as waveform randomization [5], non-linear filtering [17], whitening [18], and slow-time generative adversarial network [19]; 3) range-velocity (RV) domain MIM [20]–[23] that directly treats the RV heatmap as an image and trains neural networks as a denoiser (such as convolution-based autoencoder) to remove the interference; 4) communication-assisted MIM [24], [25]. A unified performance evaluation of a set of MIM methods can be found in [26] and [27].

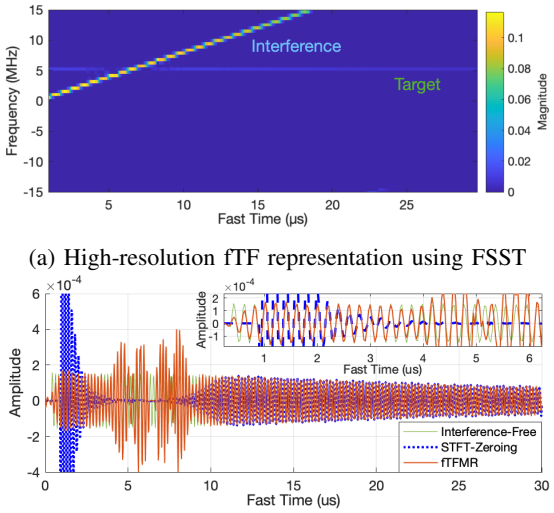

(a) High-resolution fTF representation using FSST

(b) Recovered fast-time target signals using STFT-zeroing [7] and proposed fTFMR

Fig. 1: Fast-time-frequency (fTF) representation of targets and interference, and recovered targets from interfered signals.

Here, we are particularly interested in the fast-time domain MIM as non-coherent FMCW interferences exhibit unique signatures in the fast-time-frequency (fTF) representation, as shown in Fig. 1 (a), where the sinusoidal-like target is focused on one range frequency bin while the power-dominating interference intersects the target in a form of a chirp (see Section II for explanation). Previous approaches exploit the linear chirp feature of the interference and set detected interferences to zero in the short-time Fourier transform (STFT) domain (as referred to as STFT-Zeroing) [7]. However, errors in the interference detection and zeroing steps easily propagate to the fast-time domain and it results in strong residuals, as shown in blue lines in Fig. 1 (b). This effect becomes worse when the low-resolution STFT is used [12].

Instead of focusing on nulling interferences like the most fast-time MIM methods, this paper proposes to directly recover fast-time target signals via a direct fTF mode retrieval (fTFMR). Key challenges are 1) to identify weaker target ridges among significantly stronger interference ridges that spread linearly over the fTF representation and 2) to enable high-precision fTFMR that maps the identified target-inclusive fTF representation into the fast-time sample. This is achieved

†The work of S. Jin was done during his internship at MERL.

by a cascade of high-resolution fTF representation, robust ridge detection using sequential pulses, and direct fTFMR. The advantages of the proposed method are listed below:

- First, a high-resolution fTF representation enables higher-degree separation between the target signals and interference signals. This is particularly important to the case that the interference beat frequency crosses over that of the target; see Fig. 1 (a). To this end, we make use of a frequency reassignment-based Fourier synchrosqueezing transform (FSST) [28]–[31] that enables high-resolution fTF representation.
- Second, the proposed ridge detection exploits the fact that the target signature over the fTF domain is consistent over multiple pulses, while the interference signature is highly likely to vary due to the non-coherent nature between the interfering and victim radars. This results in a robust ridge detection of underwhelmed two-way attenuated target signals among one-way attenuated interferences.
- Third, the fTFMR is guaranteed to converge to the target signal in fast-time intervals with sufficient separation between the target and interference in the fTF domain. As the FSST highly focuses on sinusoidal-like target signals, the fTFMR can directly recover target signals in the time-domain by integrating the fTR representation over the target-only region and, at the same time, filtering out interference and noise.

II. Target and Interference Signal Model

Assuming an FMCW automotive radar, indexed by u, transmits a sequence of chirp pulses with carrier frequency modulated at the radio frequency (RF) bands and a pulse repetition interval (PRI) $\widetilde{T}_u$ [2]

$$x_u^{RF}(t) = a_u^{RF} e^{j2\pi(f_0 t + 0.5 h_u t^2)}, \ \forall t \in [0, T_u] \tag{1}$$

where a_u^{RF} is the RF amplitude, f_0 is the central frequency, h_u is the chirp rate, T_u is the chirp sweep duration, and $\widetilde{T}_u - T_u$ is the inter-pulse idle duration. Without loss of generality, all automotive radars operate at the same central frequency f_0, e.g., $f_0 = 77$ GHz, but with with different chirp sweep duration T_u, PRI $\widetilde{T}_u$, and chirp rate h_u. Furthermore, the victim radar is referred to as the radar 0, i.e., $u = 0$. For the l-th chirp pulse, the dechirped signal of the victim radar is a multi-component signal

$$x_l(t) = x_l^o(t) + x_l^i(t) = \sum_{k=1}^{K^o} x_{l,k}^o(t) + \sum_{u=1}^{U_l^i} x_{l,u}^i(t), \tag{2}$$

where $x_l^o(t)$ consists of K^o target components, and $x_l^i(t)$ is the sum of U_l^i interference components. Note that the number of interferences U_l^i may vary over the pulse.

For the *target component* $x_{l,k}^o(t)$, one can derive its expression by multiplying the attenuated and delayed copy with the transmitted signal in (1) at the local oscillator, and

$$x_{l,k}^o(t) = a_k^o e^{j2\pi\phi_{l,k}^o(t)}, \ \forall t \in [0, T_0], \tag{3}$$

where a_k^o is the intermediate frequency (IF) amplitude of target k, and the phase term is given as

$$\phi_{l,k}^o(t) = (f_{r,k}^o + f_{D,k}^o)t + f_{D,k}^o(l-1)T_0, \tag{4}$$

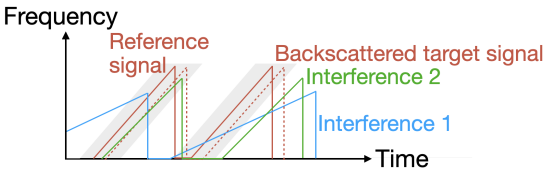

(a) RF band signal

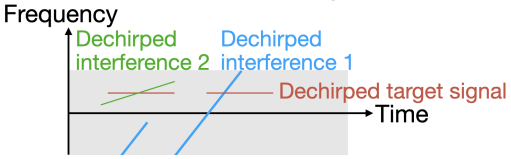

(b) IF band signal

Fig. 2: FMCW radar interferences over multiple pulses.

with $f_{r,k}^o$ and $f_{D,k}^o$ denoting the beat frequency and, respectively, the Doppler frequency of the k-th target.

On the other hand, the *interference component* may or may not be dechirped into the IF band of the victim radar, depending on FMCW configurations between the victim radar $\{f_0, h_0, T_0, \widetilde{T}_0\}$ and the u-th interfering radar $\{f_0, h_u, T_u, \widetilde{T}_u\}$ as well as their relative time offset at l-th chirp cycle $\tau_{u,l}$. The u-th interference at the l-th pulse turns out to be a chirp signal [13]

$$x_{l,u}^i(t) = a_u^i e^{j2\pi\phi_{l,u}^i(t)}, \ \forall t \in \mathcal{T}_{l,u}^i, \tag{5}$$

where a_u^i is the IF amplitude of interference u, the phase term is given as

$$\phi_{l,u}^i(t) = 0.5(h_u - h_0)t^2 - (h_u\tau_{u,l} - f_{D,u}^i)t + \phi_{l,u,0}^i, \tag{6}$$

with $f_{D,u}^i$ denoting the Doppler frequency of interference u and $\phi_{l,u,0}^i$ denoting initial phase difference between interferer and victim radar at the l-th pulse, and $\mathcal{T}_{l,u}^i$ denotes the contaminated fast-time interval of the l-th pulse due to the u-th interference

$$\mathcal{T}_{l,u}^i = \left\{ t \,\middle|\, \left|(h_u - h_0)t - (h_u\tau_{u,l} - f_{D,u}^i)\right| \le f_L \right\}, \tag{7}$$

which is determined from the fact that the interference signal $x_{l,u}^i(t)$ must lie in the IF band of the victim radar with IF bandwidth f_L. Fig. 2 provides an illustrative example of two FMCW pulses where the interfering radars yield different chirp-like interference patterns, while the target signatures in the fast-time-frequency domain remain the same.

III. Proposed Interference Mitigation Method

Our goal is to reconstruct $\mathbf{x}_l^o(t)$ from $\mathbf{x}_l(t)$. This is achieved by separating the targets from the interferences in the fTF domain via high-resolution time-frequency tools, identifying the target ridge by utilizing the consistent patterns of the target and varying patterns of the interferences, and directly reconstructing target signals via the fTFMR.

A. High-Resolution Fast-Time-Frequency Representation

For the l-th pulse, the fast-time samples of the received signal $x_l(t)$ can be transformed to the fTF representation

$X_l(t,\omega)$ via standard time-frequency analysis such as the STFT as adopted by several fast-time MIM methods [7], [14]–[16]. In contrast to these methods focusing on the interference patterns, we propose to use the FSST [28]–[31] that highly focuses on the target pattern and allows fTFMR, and directly reconstruct the fast-time target signals from the focused target portions of the fTF representation with limited inclusion of interference and noise.

The FSST can be considered as a frequency-domain reassignment of the STFT. Given the STFT of $x_l(t)$

$$V_{x_l}^g(t,\omega) = \int_{\mathbb{R}} x_l(\tau) g^*(\tau - t) e^{-i\omega\tau} d\tau, \tag{8}$$

where $g(t)$ is the time-domain window function, $(\cdot)^*$ denotes the complex conjugate, and ω is the frequency variable, its centroid (local energy) of the spectrogram, i.e., $|V_{x_l}^g(t,\omega)|^2$, can be computed as [32]

$$\hat{\omega}_{x_l}(t,\omega) = \omega - \Im\left\{ \frac{V_{x_l}^{g'}(t,\omega)}{V_{x_l}^g(t,\omega)} \right\}, \tag{9}$$

where $V_{x_l}^{g'}(t,\omega)$ denotes the STFT with the window function give by the derivative of $g(t)$, and $\Im\{\cdot\}$ takes the imaginary part of the input. The FSST reassigns the STFT from the point of computation to its centroid along the frequency (ω) domain over each fast-time instant t [28], [29]

$$X_l(t,\omega) = \frac{\int_{\mathbb{R}} V_{x_l}^g(t,v) e^{i\omega t} \delta\left(\omega - \hat{\omega}_{x_l}(t,v)\right) dv}{2\pi g^*(0)}, \tag{10}$$

where $\delta(\cdot)$ denotes the Dirac function. As detailed analyzed in [30], the FSST-based fTFR highly focuses on sinusoid-like target signals; see Fig.1 (a) for an illustration.

B. Robust Ridge Detection of Underwhelmed Targets

Reconstructing the target $x_{l,k}^o(t) = a_{l,k}^o e^{j2\pi\phi_{l,k}^o(t)}$ requires separating it from interferences and other target signals. This can be done by detecting its ridge $\Omega_{l,k}^o(t)$ in the fTF domain, i.e., the estimation of its instantaneous frequency $d\phi_{l,k}^o(t)/dt$. As each target is a single-tone signal (as shown in (4)), the target ridge $\Omega_{l,k}^o(t)$ is a constant function of t and is a straight line in the fTF representation. As shown in Fig. 3 (a) and (b), the target ridge stays the same over the multiple pulses within a coherent processing interval (CPI), while the FMCW interference ridges are likely to vary over multiple pulses due to the non-coherence between the interfering and victim radars.

The above observation leads us to propose a multi-pulse ridge detection method, given in Fig. 3 (c). It first deploys, at each pulse, a maximum-energy ridge detector that uses a penalized forward-backward greedy algorithm [33] to sequentially detect the strongest signal ridge. The detected target ridges are denoted as $\Omega_{l,k}^d(t)$. Fig. 3 (a) and (b) show the detected target ridges when there is only a target in a pulse and, respectively, when there are two interference signals and one target in another pulse. It is noted that the detected ridges may be a mixture of targets and interference.

Next, we validate whether the detected ridges indeed correspond to the target, and correct them using confirmed target

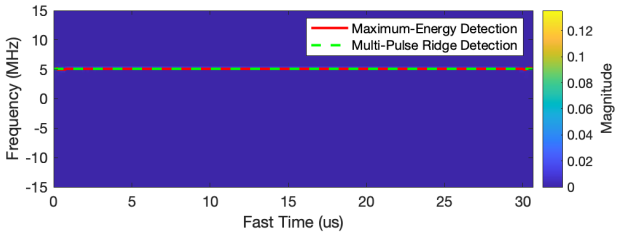

(a) fTF representation and ridge detection in a pulse

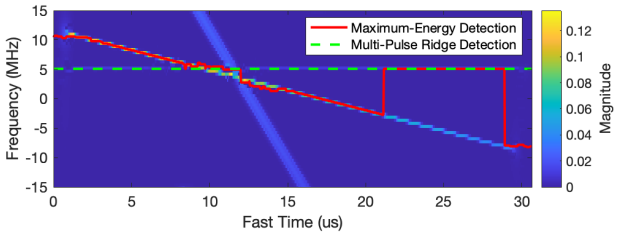

(b) fTF representation and ridge detection in another pulse

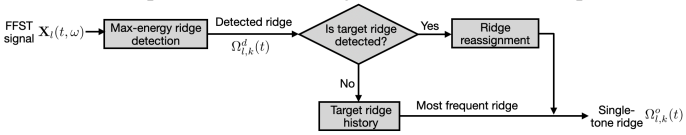

(c) Flow chart of proposed multi-pulse ridge detection

Fig. 3: Robust ridge detection exploits consistent target signatures and varying interference signatures from multiple pulses.

ridges from other pulses in the same CPI if necessary. We first validate the detected ridges by checking if

$$\sum_{n=1}^{N} \mathbf{1}\big(\Omega_{l,k}^d(n\Delta T) = \text{mode}(\{\Omega_{l,k}^d(n\Delta T), n = 1,\ldots,N\})\big) > N^{TH}, \tag{11}$$

where N is the number of time bins in the fTF domain, ΔT is the time resolution of the fTF such that $N\Delta T = T_0$, mode$(\cdot)$ means the value that appears the most often in a set of values, N^{TH} is a threshold.

- If the target ridge is *detected*, we reassign the target ridge to be a constant function over the fast time with the beat frequency equal to the most frequent bin of the detected ridge:

$$\Omega_{l,k}^o(t) = \text{mode}(\{\Omega_{l,k}^d(n\Delta T), n = 1,\ldots,N\}). \tag{12}$$

- If the target ridge is *not* detected, we resort to the history of the most frequent ridge over multiple pulses in the same CPI and assign it to the target ridge in this pulse l,

$$\Omega_{l,k}^o(t) = \text{mode}(\{\Omega_{l',k}^o(t), l' = [1,\ldots,L]\backslash\{l\}\}), \tag{13}$$

where L is the number of pulses in a CPI. For instance of Fig. 3 (b), the detected ridge $\Omega_{l,k}^d(t)$ fails to pass the validation of (11) and the target ridge is re-assigned by looking into the target ridges from other pulses.

C. Fast-Time-Frequency Mode Retrieval of Targets

The final step is to directly reconstruct the target signal $x_{l,k}^o(t)$ from its fTF representation $X_l(t,\omega)$ and the detected target ridge $\Omega_{l,k}^o(t), k = 1,2,\ldots,K^o$. To avoid introducing

interference component on the target ridge $\Omega_{l,k}^o(t)$, the fTFMR uses the interference-free time region along the detected ridges

$$\hat{X}_{l,k}(t,\omega) = \begin{cases} X_l(t,\omega), & t \in \hat{\mathcal{T}}_{l,k}^o(\omega), |\omega - \Omega_{l,k}^o(t)| < \epsilon, \\ 0, & \text{otherwise}, \end{cases}$$

where $\hat{\mathcal{T}}_{l,k}^o(\omega)$ is the estimated interference-free time region of the target ridge k. Then, the fTFMR directly integrates $\hat{X}_{l,k}(t,\omega)$ over a small frequency interval around $\Omega_{l,k}^o(t)$:

$$\hat{x}_{l,k}^o(t) = \frac{1}{g(0)} \int_{|\omega - \Omega_{l,k}^o(t)| < \epsilon} \hat{X}_{l,k}(t,\omega) d\omega, \tag{14}$$

where $\hat{x}_{l,k}^o(t)$ is the reconstructed fast-time signal of target k.

To obtain $\hat{\mathcal{T}}_{l,k}^o(\omega)$, one can estimate the interference-free time bins on $\mathcal{X}_l(\omega) \triangleq \{|X_l(n\Delta T,\omega)|^2, n = 1,2,\ldots,N\}$ for each frequency bin satisfying $\{\omega : |\omega - \Omega_{l,k}^o(t)| < \epsilon\}$ using the median absolute deviation (MAD) detector [34]. The MAD detector estimates the interference-free time bin $o \in \mathcal{O}_{l,k}$ if

$$\begin{aligned} &||X_l(o\Delta T,\omega)|^2 - \text{median}(\mathcal{X}_l(\omega))| < \\ &\gamma^{MAD} \underset{i=1,2,\ldots,N}{\text{median}} (||X_l(i\Delta T,\omega)|^2 - \text{median}(\mathcal{X}_l(\omega))|). \end{aligned}$$

The MAD detector is used to ensure the outliers on the target ridge (regarded as interference) are excluded as much as possible. Then, the interference-free time region of the target k is estimated as

$$\hat{\mathcal{T}}_{l,k}^{MAD}(\omega) = \bigcup_{o \in \mathcal{O}_{l,k}} [(o-1)\Delta T, o\Delta T]. \tag{15}$$

Furthermore, to retain the target portion as much as possible, one can compare each element in $\mathcal{X}_l(\omega)$ with the power profile of target k, i.e., $\mathcal{P}_{l,k} = \{|X_{l'}(n\Delta T,\omega)|^2, n = 1,\ldots,N,\ l' = 1,\ldots,l-1\}$, and determine the set of time bins corresponding to target k

$$\mathcal{Q}_{l,k} = \{q : |X_l(q\Delta T,\omega)|^2 < \gamma^{His} \text{median}(\mathcal{P}_{l,k})\}, \tag{16}$$

where γ^{His} is the target detection threshold in the power profile. Then, the interference-free portion of the target k is estimated as

$$\hat{\mathcal{T}}_{l,k}^{His}(\omega) = \bigcup_{q \in \mathcal{Q}_{l,k}} [(q-1)\Delta T, q\Delta T]. \tag{17}$$

Finally, we combine the results in (15) and (17), and obtain the estimated interference-free portion for target k as

$$\hat{\mathcal{T}}_{l,k}^o(\omega) = \hat{\mathcal{T}}_{l,k}^{MAD}(\omega) \cup \hat{\mathcal{T}}_{l,k}^{His}(\omega). \tag{18}$$

Denoting $\mathcal{T}_{l,k}^o(\omega)$ as the true interference-free time region of the target k on frequency ω, we have the following performance guarantee of the mode reconstruction.

Theorem 1 (Reconstruction Performance Guarantee): There exists a constant C such that for all $t \in \bigcap_{\omega: \left|\omega - \frac{d\phi_{l,k}^o(t)}{dt}\right| < \epsilon} \mathcal{T}_{l,k}^o(\omega)$,

$$\left| \frac{1}{g(0)} \int_{\left|\omega - \frac{d\phi_{l,k}^o(t)}{dt}\right| < \epsilon} X_l(t,\omega) d\omega - x_{l,k}^o(t) \right| \le C\epsilon. \tag{19}$$

Proof: By [28], for all interference-free time $\bigcap_{\omega: \left|\omega - \frac{d\phi_{l,k}^o(t)}{dt}\right| < \epsilon} \mathcal{T}_{l,k}^o(\omega)$, (19) holds for target k. ■

Theorem 1 indicates that, when the detected ridge $\Omega_{l,k}^o(t)$ is close to the instantaneous frequency $d\phi_{l,k}^o(t)/dt$ and the estimated interference-free time region $\hat{\mathcal{T}}_{l,k}^o(\omega)$ is close to the real interference-free time region $\mathcal{T}_{l,k}^o(\omega)$, the reconstructed signal $\hat{x}_{l,k}^o(t)$ given by (14) is a good estimator of original target signal $x_{l,k}^o(t)$.

IV. Performance Evaluation

In this section, we provide numerical evaluation of the proposed fTFMR-based MIM method using synthetic data generated corresponding to a typical medium-range automotive radar configurations [35]. Moreover, we include the following baseline methods for performance comparison.

- Time-domain zeroing (Time-Zeroing) [26], [27]: The victim radar detects interference in the fast-time domain and nulls the interference.
- Iterative method with adaptive thresholding (IMAT) [10]: IMAT is based on Time-Zeroing and employs a sparse sampling procedure to reconstruct the contaminated fast-time samples from the uncontaminated portion.
- STFT-Zeroing [7]: STFT-Zeroing detects interference in the STFT-based fTF representation using a cell-average constant false alarm rate (CA-CFAR) detector, removes the interference, and finally transforms the modified fTF representation back to the fast-time domain.

We also include the interference-free and no mitigation to set the best and worse performance benchmarks.

A. Simulation Setup

We consider a scenario of 1 non-fluctuating target and 1 victim radar with FMCW configuration parameters given in Table I for a typical automotive radar operating in 77 GHz [35]. In the same scenario, we consider strong interference and include 5 close interferers with relative distances to the victim radar, chirp rates, and inter-chirp idle duration randomly (uniformly) distributed according to the last three rows of Table I.

TABLE I: Simulation setup parameters.

Transmit power (noise figure)	5dBm (4.5dB)
Transmit (receive) antenna gain	36(42)dBi
RF frequency	77GHz
Chirp bandwidth	460MHz
Victim radar's chirp sweep duration	30.7us
Victim radar's inter-chirp idle duration	7us
Victim radar's chirp slope	15MHz/us
IF bandwidth (ADC complex sample rate)	15MHz (16.7 MHz)
Number of chirps in a CPI	256
Range (Velocity) DFT size	512 (256)
Radar detector	2D CA-CFAR
CA-CFAR training (guard) size	5 (3) for row & column
Target model	Non-fluctuating
Target's RCS	20dBsm
Target's distance (velocity)	50m (12.1m/s)
Target (interference) channel	Free-space two-way (one-way) channel
Interferer's distance	$U(0,10)$m
Interferer's chirp rate	$U(10,20)$MHz/us
Interferer's inter-chirp idle duration	$U(6,8)$us

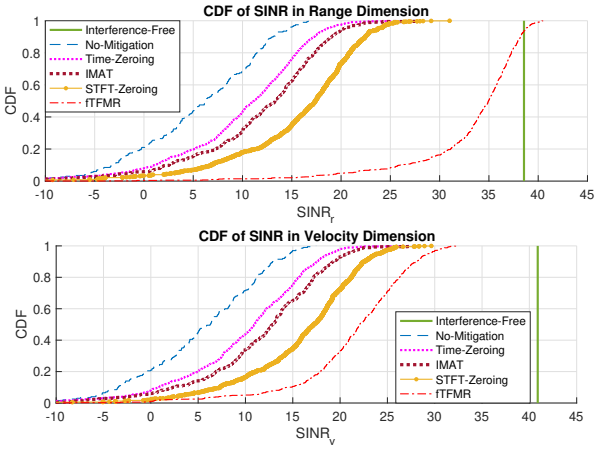

Fig. 4: CDFs of SINR_r and SINR_v.

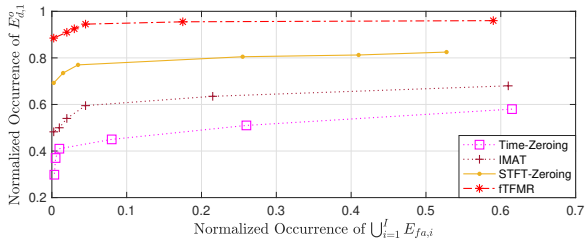

Fig. 5: Target detection counts on target bins and false detection counts on non-target bins normalized over 200 Monte-Carlo runs.

The synthetic data is generated using a system-level simulator based on MATLAB Phased Array System Toolbox. It consists of the FMCW waveform generation, the backscattering of the FMCW waveform from a target, interference channel propagation, and a standard FMCW signal processing (e.g., dechirping, low-pass filtering, range-velocity processing and CFAR detection, etc.) at the receiver.

Simulation parameters are chosen as follows. For the proposed fTFMR method, the FSST uses a Kaiser window of length 256 and shape parameter 10 and an overlapping size of 255, while $N^{TH} = 3/8N$, $\gamma^{His} = 2.5$, ϵ is the width of 4 frequency bins in fTF domain, and the threshold for the MAD detection is 1.2. For the baseline methods, the threshold of the MAD detection is 4.4 for the Time-Zeroing and IMAT methods. The STFT-Zeroing uses a Hann window of length 128, an overlapping size of 96, and an FFT length of 256.

B. Performance Measures

The following performance measures are used for performance comparison.

- SINR in range dimension, $SINR_r$:

$$SINR_r = \frac{|\mathbf{S}^{RV}[n_o, m_o]|^2}{\sum\limits_{n \in \mathcal{N}_r \setminus \{n_o\}} |\mathbf{S}^{RV}[n, m_o]|^2/(N_r - 1)}, \quad (20)$$

where $\mathbf{S}^{RV}$ is the RV spectrum after RV FFT, $\mathcal{N}_r$ is the set of range bins and $N_r = |\mathcal{N}_r|$.

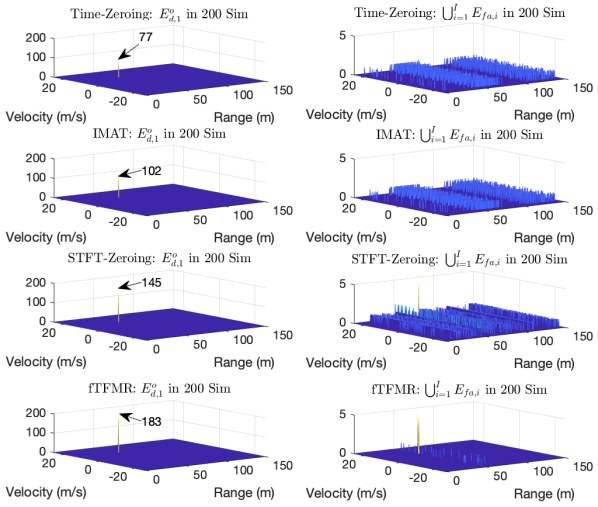

Fig. 6: Heatmap of detection counts on the range-velocity domain over 200 Monte-Carlo runs.

- SINR in velocity dimension, $SINR_v$:

$$SINR_v = \frac{|\mathbf{S}^{RV}[n_o, m_o]|^2}{\sum\limits_{m \in \mathcal{M}_v \setminus \{m_o\}} |\mathbf{S}^{RV}[n_o, m]|^2/(M_v - 1)}, \quad (21)$$

where $\mathcal{M}_v$ is the set of velocity bins and $M_v = |\mathcal{M}_v|$.

- *Target detection counts* on target bins are defined as the occurrence of $\bigcap_{k=1}^{K^o} E^o_{d,k}$ over Monte-Carlo runs, where $E^o_{d,k}$ is the event that the radar's CFAR detector detects a peak on its range-velocity bin, given that target k exists on this range-velocity bin.
- *False detection counts* on non-target bins are defined as the occurrence of $\bigcup_{i=1}^{I} E_{fa,i}$ over Monte-Carlo runs, where I is the total number of detected peaks, and $E_{fa,i}$ is defined similarly as $E^o_{d,k}$ except that the peak i does not corresponds to a target.

It is worth noting that $SINR_r$ and $SINR_v$ are the two measures widely used in the literature [26].

C. SINR Comparison

Fig. 4 shows the cumulative distribution function (CDF) of $SINR_r$ and $SINR_v$ over 1000 Monte-Carlo runs. It is seen that all considered MIM methods outperform the case of No-Mitigation. The Time-Zeroing and IMAT methods provide similar performance, as previously observed in [26] and [27]. It is clear to see that the proposed fTFMR method achieves higher $SINR_r$ and $SINR_v$ than all baseline methods. It is interesting to note that the fTFMR also filters out the noise that spreads over the fTF domain as (14) integrates only the fTF portion confined to the target. This may lead to a higher $SINR_r$ than that of the Interference-Free case as the denominator of (20) is smaller for the fTFMR method. Comparing Fig. 4 (a) and Fig. 4 (b) reveals that the SINR gain in the range domain is larger than that in the velocity domain as the current fTFMR method only mitigates the interference in the fast-time (range) domain.

D. Detection Performance Comparison

Fig. 5 plots the normalized occurrence of $E^o_{d,1}$ versus the normalized occurrence of $\bigcup_{i=1}^{I} E_{fa,i}$ over 200 Monte-Carlo runs of randomly simulated interference. For each method, the curve is obtained by changing the threshold used in the 2D (range-velocity) CA-CFAR detection. The result shows that the fTFMR method outperforms the baseline methods in terms of target detection and false alarm rate.

To visualize the detection and false alarm performance, Fig. 6 plot the heatmap of the occurrence of $E^o_{d,1}$ and $\bigcup_{i=1}^{I} E_{fa,i}$ over the range-velocity domain. For each method, we run the 2D CA-CFAR detection over all range-velocity bins and report the total counts of detection as a 2D heatmap. In the left column, the total counts over the true target bin are reported, where the fTFMR method gives the highest counts of detection. The right column, on the other hand, reports the total counts over all non-target bins which represents a qualitative assessment of the false detection distribution over the RV domain. It is clear to see that the fTFMR method shows a cleaner false alarm heatmap than other methods.

V. Conclusion

We considered non-coherent FMCW radar interference mitigation. Specifically, we proposed to use a high-resolution fast-time-frequency transform to have a better separation between the target and interference, robust ridge detection of underwhelmed target by using information from multiple chirp pulses, and a direct fTF mode retrieval. Comprehensive performance comparison confirms significant performance gain of the proposed method over a long list of baseline methods.

References

[1] D. Guermandi *et al.*, "A 79-GHz 2 × 2 MIMO PMCW Radar SoC in 28-nm CMOS," *IEEE Journal of Solid-State Circuits*, vol. 52, no. 10, pp. 2613–2626, 2017.

[2] C. Aydogdu *et al.*, "Radar interference mitigation for automated driving: Exploring proactive strategies," *IEEE Signal Processing Magazine*, vol. 37, no. 4, pp. 72–84, 2020.

[3] P. Wang, D. Millar, K. Parsons, R. Ma, and P. V. Orlik, "Range accuracy analysis for FMCW systems with source nonlinearity," in *ICMIM*, 2019, pp. 1–5.

[4] P. Wang, P. Boufounos, H. Mansour, and P. V. Orlik, "Slow-time MIMO-FMCW automotive radar detection with imperfect waveform separation," in *ICASSP*, 2020, pp. 8634–8638.

[5] S. Jin and S. Roy, "FMCW radar network: Multiple access and interference mitigation," *IEEE Journal of Selected Topics in Signal Processing*, vol. 15, no. 4, pp. 968–979, 2021.

[6] Y. Xia, P. Wang, K. Berntorp, L. Svensson, K. Granström, H. Mansour, P. Boufounos, and P. V. Orlik, "Learning-based extended object tracking using hierarchical truncation measurement model with automotive radar," *IEEE Journal of Selected Topics in Signal Processing*, vol. 15, no. 4, pp. 1013–1029, 2021.

[7] J. Wang, "CFAR-based interference mitigation for FMCW automotive radar systems," *arXiv:2101.01257*, 2021.

[8] M. Barjenbruch *et al.*, "A method for interference cancellation in automotive radar," in *ICMIM*, 2015, pp. 1–4.

[9] F. Jin and S. Cao, "Automotive radar interference mitigation using adaptive noise canceller," *IEEE Transactions on Vehicular Technology*, vol. 68, no. 4, pp. 3747–3754, 2019.

[10] J. Bechter, F. Roos, M. Rahman, and C. Waldschmidt, "Automotive radar interference mitigation using a sparse sampling approach," in *2017 European Radar Conference (EURAD)*, 2017, pp. 90–93.

[11] S. Lee, J.-Y. Lee, and S.-C. Kim, "Mutual interference suppression using wavelet denoising in automotive FMCW radar systems," *IEEE Trans. on Intelligent Transportation Systems*, vol. 22, no. 2, pp. 887–897, 2021.

[12] A. Correas-Serrano and M. A. Gonzalez-Huici, "Sparse reconstruction of chirplets for automotive FMCW radar interference mitigation," in *ICMIM*, 2019, pp. 1–4.

[13] F. Uysal and S. Sanka, "Mitigation of automotive radar interference," in *RadarConf*, 2018, pp. 0405–0410.

[14] N.-C. Ristea, A. Anghel, and R. T. Ionescu, "Fully convolutional neural networks for automotive radar interference mitigation," in *2020 IEEE 92nd Vehicular Technology Conference (VTC2020-Fall)*, 2020, pp. 1–5.

[15] J. Wang, R. Li, Y. He, and Y. Yang, "Prior-guided deep interference mitigation for FMCW radars," *arXiv:2108.13023*, 2021.

[16] S. Neemat, O. Krasnov, and A. Yarovoy, "An interference mitigation technique for FMCW radar using beat-frequencies interpolation in the stft domain," *IEEE Transactions on Microwave Theory and Techniques*, vol. 67, no. 3, pp. 1207–1220, 2019.

[17] M. Wagner *et al.*, "Threshold-free interference cancellation method for automotive FMCW radar systems," in *2018 IEEE International Symposium on Circuits and Systems (ISCAS)*, 2018, pp. 1–4.

[18] M. Toth, P. Meissner, A. Melzer, and K. Witrisal, "Slow-time mitigation of mutual interference in chirp sequence radar," in *ICMIM*, 2020, pp. 1–4.

[19] S. Chen *et al.*, "Automotive radar interference mitigation based on a generative adversarial network," in *2020 IEEE Asia-Pacific Microwave Conference (APMC)*, 2020, pp. 728–730.

[20] J. Fuchs *et al.*, "Automotive radar interference mitigation using a convolutional autoencoder," in *2020 IEEE International Radar Conference (RADAR)*, 2020, pp. 315–320.

[21] C. Jiang, T. Chen, and B. Yang, "Adversarial interference mitigation for automotive radar," in *RadarConf*, 2021, pp. 1–6.

[22] A. Dubey *et al.*, "Region based single-stage interference mitigation and target detection," in *RadarConf*, 2020, pp. 1–5.

[23] J. Rock, W. Roth, M. Toth, P. Meissner, and F. Pernkopf, "Resource-efficient deep neural networks for automotive radar interference mitigation," *IEEE Journal of Selected Topics in Signal Processing*, vol. 15, no. 4, pp. 927–940, 2021.

[24] C. Aydogdu, M. F. Keskin, N. Garcia, H. Wymeersch, and D. W. Bliss, "Radchat: Spectrum sharing for automotive radar interference mitigation," *IEEE Transactions on Intelligent Transportation Systems*, vol. 22, no. 1, pp. 416–429, 2021.

[25] K. U. Mazher, R. W. Heath, K. Gulati, and J. Li, "Automotive radar interference characterization and reduction by partial coordination," in *RadarConf*, 2020, pp. 1–6.

[26] M. Toth, P. Meissner, A. Melzer, and K. Witrisal, "Performance comparison of mutual automotive radar interference mitigation algorithms," in *RadarConf*, 2019, pp. 1–6.

[27] M. Toth, J. Rock, P. Meissner, A. Melzer, and K. Witrisal, "Analysis of automotive radar interference mitigation for real-world environments," in *2020 17th European Radar Conference (EuRAD)*, 2021, pp. 176–179.

[28] T. Oberlin, S. Meignen, and V. Perrier, "The Fourier-based synchrosqueezing transform," in *2014 IEEE International Conference on Acoustics, Speech and Signal Processing (ICASSP)*, 2014, pp. 315–319.

[29] F. Auger *et al.*, "Time-frequency reassignment and synchrosqueezing: An overview," *IEEE Signal Processing Magazine*, vol. 30, no. 6, pp. 32–41, 2013.

[30] G. Thakur and H.-T. Wu, "Synchrosqueezing based recovery of instantaneous frequency from nonuniform samples," *SIAM J. Math. Anal.*, vol. 43, no. 5, pp. 2078–2095, 2011.

[31] G. Thakur, E. Brevdo, N.S.Fuckar, and H.-T. Wu, "The synchrosqueezing algorithm for time-varying spectral analysis: Robustness properties and new paleoclimate applications," *Signal Processing*, vol. 93, no. 5, pp. 1079–1094, 2013.

[32] F. Auger and P. Flandrin, "Improving the readability of time-frequency and time-scale representations by the reassignment method," *IEEE Transactions on Signal Processing*, vol. 43, no. 5, pp. 1068–1089, 1995.

[33] R. Carmona, W. Hwang, and B. Torresani, "Characterization of signals by the ridges of their wavelet transforms," *IEEE Transactions on Signal Processing*, vol. 45, no. 10, pp. 2586–2590, 1997.

[34] P. J. Rousseeuw and C. Croux, "Alternatives to the median absolute deviation," *Journal of the American Statistical association*, vol. 88, no. 424, pp. 1273–1283, 1993.

[35] K. Ramasubramanian and B. Ginsburg, "AWR1243 sensor: Highly integrated. 76–81GHz radar front-end for emerging ADAS applications," *Texas Instruments Technical Report*, 2017.